Environmental Science & Technology

pubs.acs.org/est

Article

Enhanced Arsenate Immobilization by Kaolinite via Heterogeneous Pathways during Ferrous Iron Oxidation

Xin Wang, Shengyan Pu,* Jiaqi Ding, Jing Chen, Peng Liao, Delai Zhong, Daniel C. W. Tsang, John C. Crittenden, and Linling Wang*

Cite This: *Environ. Sci. Technol.* 2024, 58, 12123−12134

Read Online

ACCESS | Metrics & More | Article Recommendations | Supporting Information

ABSTRACT: Clay minerals are ubiquitous in subsurface environments and have long been recognized as having a limited or negligible impact on the fate of arsenic (As) due to their negatively charged surfaces. Here, we demonstrate the significant role of kaolinite (Kln), a pervasive clay mineral, in enhancing As(V) immobilization during ferrous iron (Fe(II)) oxidation at near-neutral pH. Our results showed that Fe(II) oxidation alone was not capable of immobilizing As(V) at relatively low Fe/As molar ratios (≤2) due to the generation of Fe(III)−As(V) nanocolloids that could still migrate easily as truly dissolved As did. In the presence of kaolinite, dissolved As(V) was significantly immobilized on the kaolinite surfaces via forming Kln−Fe(III)−As(V) ternary precipitates, which had large sizes (at micrometer levels) to reduce the As mobility. The kaolinite-induced heterogeneous pathways for As(V) immobilization involved Fe(II) adsorption, heterogeneous oxidation of adsorbed Fe(II), and finally heterogeneous nucleation/precipitation of Fe(III)−As(V) phases on the edge surfaces of kaolinite. The surface precipitates were mixtures of amorphous basic Fe(III)−arsenate and As-rich hydrous ferric oxide. Our findings provide new insights into the role of clay minerals in As transformation, which is significant for the fate of As in natural and engineered systems.

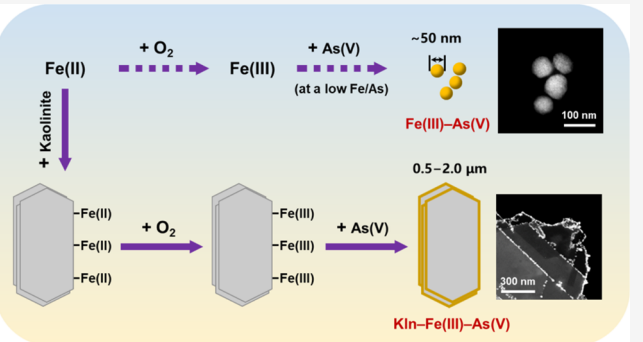

KEYWORDS: *arsenic immobilization, ferrous iron oxidation, colloids, kaolinite edge sites, heterogeneous pathways*

INTRODUCTION

Arsenic (As) contamination in groundwater and soil is a great concern worldwide. The mobility and toxicity of As in subsurface environments are often controlled by the interaction with iron (Fe).[1] When contacted with oxygen, Fe(II) is oxidized to Fe(III) and then hydrolyzes and nucleates *in situ* to create Fe(III)−As coprecipitates in the presence of As.[2−4] The transformation of dissolved As to solid phases is deemed to immobilize As and reduce its environmental risks, while the effectiveness depends on the physicochemical characteristics of Fe−As coprecipitates, such as particle sizes.[4−6] If *in situ* coprecipitation of Fe and As forms nanosized colloids, the mobility of As would not be reduced because nanocolloidal As could transport faster than dissolved As in groundwater.[7]

The size and composition of Fe−As coprecipitates could be influenced by coexisting components in subsurface environments. For example, the presence of dissolved organic matter (DOM) may induce the formation of stable and small DOM−Fe−As colloids resulting in a higher mobility of As.[8−10] In contrast, coexisting cations like Ca^{2+} and Mg^{2+} can lead to the formation of large clusters/aggregates to enhance As immobilization, via Ca/Mg−As−Fe ternary interactions and surface charge modification.[5,11] Clay minerals are ubiquitous in subsurface and have a significant impact on the fate of cationic metals,[12] whereas their impacts on the formation of Fe−As coprecipitates and the resulting mobility of As remain unknown.

In general, clay minerals are sensitive to cations but inert to oxyanions due to their basal surfaces with permanent negative charges and edge surfaces with variable negative charges at near-neutral pH.[13,14] Positively charged cations such as Fe(II), Cd(II), Cu(II), Ni(II), Pb(II), and Zn(II) are all readily adsorbed onto clay mineral surfaces through surface complexation and/or cation exchange.[15,16] On the contrary, the adsorption of oxyanions (like As and P) onto clay minerals is limited or even negligible.[17,18] Recently, Fakhreddine and Fendorf reported that the presence of cations (e.g., K^+, Ca^{2+}, and Mg^{2+}) could enhance As adsorption on clay minerals via

Received: February 25, 2024
Revised: June 18, 2024
Accepted: June 20, 2024
Published: June 27, 2024

forming cation bridging outer-sphere complexes.[19] If Fe^{2+} encounters arsenate oxyanions and clay minerals, especially in the presence of oxygen, the situation will be more intricate than those faced by K^+, Ca^{2+}, and Mg^{2+}. Considering the redox property of Fe^{2+} and the high affinity of iron for arsenic,[20,21] clay−Fe−As ternary products may generate where Fe acts as a bridge. Unlike DOM−Fe−As colloids mentioned above, the formed clay−Fe−As may have relatively large particle sizes of up to several micrometers because of the intrinsic sizes of clay minerals (e.g., kaolinite),[22] thus mitigating the mobility of As. Accordingly, the role of clay minerals in As immobilization may be underestimated.

In order to investigate the role of clay minerals in As(V) immobilization during Fe(II) oxidation, clay&Fe(II)&As(V) ternary systems were compared with Fe(II)&As(V) binary systems under oxic conditions in batch experiments. Kaolinite (Kln), which is widely distributed in tropical and subtropical regions,[23] was selected as the model clay mineral. The investigated systems are relevant to anoxic groundwater containing Fe(II) and arsenate when brought into contact with O_2, for example, by groundwater table fluctuation.[24] Overall, the main objectives are to evaluate the immobilization of As(V) in the presence of kaolinite during Fe(II) oxidation and to reveal the mechanisms of kaolinite-controlled As immobilization in the Kln&Fe(II)&As(V) ternary system with oxygen.

MATERIALS AND METHODS

Materials and Chemicals. Kaolinite (#03584) from Sigma-Aldrich was chosen as a model mineral, and $Na_2HAsO_4{\cdot}7H_2O$ (≥98%) from Sigma-Aldrich was used for the preparation of As(V) solution. 2-(*N*-morpholino)-ethanesulfonic acid monohydrate (MES, ≥99%) and 3-(*N*-morpholino)propanesulfonic acid (MOPS, ≥99%) from Aladdin were selected as noncomplexing buffers, which have been widely used in Fe(II) oxidation and metal ion adsorption-related studies.[25] Other chemicals used in this study are described in Text S1 of the Supporting Information (SI). The physicochemical properties of kaolinite are summarized in Table S1.

Arsenate Immobilization Experiments. Batch experiments were conducted to investigate the immobilization of As(V) during Fe(II) oxidation in the absence and presence of kaolinite. Most of the batch experiments were performed in magnetically stirred reactors at a speed of 500 rpm to ensure a saturated dissolved oxygen (DO) (i.e., 8.1 ± 0.2 mg/L) solution throughout the reaction. In a typical reaction, 200 μM Fe(II) were added into a 100 μM As(V) solution with 10 g/L of kaolinite (if present) that was buffered with 10 mM MOPS for pH 7.0 to initiate the reaction. NaOH (1 M) or HCl (1 M) was used to adjust the pH of As(V) solutions that contained buffers, and NaCl (1 M) was applied to control the ionic strength (IS) to 0.01 M. A 0.45 μm filter was employed for solid−liquid separation to assess As(V) immobilization in the absence and presence of kaolinite. At predetermined time intervals, samples that were filtered by 0.45 μm filters were added (1) into a 1 M HCl solution for As analyses, (2) into a phenanthroline solution for Fe(II) analyses, and (3) into a 6 M HCl solution for Fe(tot) analyses. Hydrochloric acid acidification and phenanthroline complexation are able to quench further reaction between Fe(II) and oxygen.[26] At the same time, unfiltered samples were directly mixed with phenanthroline solutions for the analyses of total Fe(II) (the sum of dissolved and adsorbed Fe(II)). Moreover, 0.02 μm filters (Whatman Anotop) were used to remove possible nano-colloidal particles in the 0.45 μm filtrates for the analysis of truly dissolved As, Fe(II), and Fe(tot).

In order to further explore the effects of kaolinite concentrations, DO concentrations, pH, and initial Fe(II)/As molar ratios on As immobilization, additional experiments under various conditions were conducted (as summarized in Table S2). In brief, kaolinite concentrations were set to 0, 1, and 10 g/L; DO concentrations were set to 0.4 and 8.1 mg/L; pH values were set to 6.0, 7.0, and 8.0; and initial Fe(II)/As molar ratios were set to 1, 2, 3, and 4. 10 mM MES were used as the buffer for pH 6.0 solutions, while 10 mM MOPS were for pH 7.0 and 8.0 solutions. To maintain a low DO condition of 0.4 mg/L during reactions, the test solutions were purged with a gas mixture with 1% oxygen and 99% nitrogen until all Fe(II) was completely oxidized.[27] And before Fe(II) addition, the solutions were purged with the gas mixture for at least 2 h to get an initial DO concentration of 0.4 mg/L. In addition, adsorption isotherm experiments under anoxic conditions were conducted to determine the adsorption capacity of kaolinite to Fe(II) in the absence and presence of As(V) (Text S2).

Analytical Methods. Arsenic concentrations in filtered samples after acidification were analyzed by inductively coupled plasma optical emission spectrometry (ICP-OES) with an Optima 8300 system (PerkinElmer), with a detection limit of 1 μM. Fe(II) concentrations in filtered samples were measured by the 1,10-*o*-phenanthroline analytical method at 510 nm using a UV−vis spectrophotometer (Evolution 201, Thermo). Total iron (Fe(tot)) was assayed through reduction of Fe(III) to Fe(II) using hydroxylamine-HCl, and the concentration of Fe(III) was calculated by the difference between Fe(II) and Fe(tot). The detection limit of Fe(II) was 0.5 μM. The total Fe(II) in unfiltered samples was determined by the direct reaction of dissolved and adsorbed Fe(II) with phenanthroline, in which all Fe(II) were transformed into soluble Fe(II)−phenanthroline complex.[28] In the suspensions containing kaolinite, the effect of particle scattering on the absorbance of the Fe(II)−phenanthroline complex was significant, and thus kaolinite was filtered by 0.45 μm filters before absorbance measurements. In the suspensions without kaolinite, the effect of particle scattering on absorbance was negligible; therefore, additional filtration was unnecessary. High mass recoveries of total Fe(II) (95−100%) were reached for all suspension samples.

General Characterization. The dynamic heterogeneous precipitation of Fe and As on kaolinite surfaces was characterized by *in situ* attenuated total reflectance Fourier transform infrared spectroscopy (ATR-FTIR, Nicolet IS50, ThermoFisher) that was equipped with a diamond internal reflection element and a mercury−cadmium−telluride detector (Text S3). Structural and morphological characterizations were conducted by using a spherical-aberration-corrected (Cs) transmission electron microscope operated at 200 kV (Titan G^2 60-300, FEI, The Netherlands) in scanning transmission electron microscopy (STEM) mode. To minimize the effect of specimen drift, the drift-correction mode was used during the acquisition of energy-dispersive spectroscopy (EDS) maps. Mineralogical composition was characterized by powder X-ray diffraction (XRD) analysis (XRD-7000, Shimadzu, Japan) with a copper target (Cu Kα). The equipment was operated by step-scanning from 10 to 80° with a scan speed of 5°/min at 40 kV and 30 mA. Surface properties were characterized by X-

https://doi.org/10.1021/acs.est.4c01976
Environ. Sci. Technol. 2024, 58, 12123−12134

ray photoelectron spectroscopy (XPS, AXIS-ULTRA DLD-600W, Shimadzu, Japan) with a monochromatic Mg Kα source. The charge effect was corrected using the C 1s line at 284.8 eV, and the curve-fitting program XPSPEAK 4.1 was applied to fitting the spectra. Particle size distribution (PSD) and ζ-potential were measured by a Zetasizer (Nano ZS90, Malvern, U.K.), in which a DTS0012 cell was used for PSD measurements and a DTS1060 folded capillary cell was used for ζ-potential measurements.

Synchrotron X-ray Absorption Spectroscopy. A total of about 100 mg of solid were collected onto a filter membrane for each X-ray absorption spectroscopy (XAS) measurement. Iron and As K-edge X-ray absorption spectra were collected at the 1W1B beamline of the Beijing Synchrotron Radiation Facility (BSRF, China). The monochromator was calibrated by setting the first inflection point in the K-edge absorption spectrum of an Fe foil to 7112 eV (Fe measurements) or the first inflection point in the L3-edge absorption spectrum of a Au foil to 11,919 eV (As measurements). Sample spectra were collected at room temperature and ambient pressure using fluorescence mode over the energy range of 6910−7910 eV (Fe) or 11,660−12,600 eV (As). Three to four scans were recorded for each sample and averaged.

Data reduction and analyses were performed with the software code Athena.[29] The Autobk algorithm was applied for background removal using a linear pre-edge line between 200 and 50 eV before the edge, E_0 (7127 eV for Fe and 11873 eV for As), and a normalization range from 170 to 750 eV (Fe) and from 170 to 760 eV (As). By default, a second-order polynomial was used as a post-edge line. The frequency cutoff parameter R_{bkg} was set to 0.95 (Fe) or 0.8 (As). The k-weight in the background function determination was set to 2 (Fe) or 3 (As). Fourier transforms of normalized k^3-weighted $\chi(k)$ data were calculated over k-ranges of 3−11 Å^{-1} (Fe) or 3−13.5 Å^{-1} (As) using a Kaiser−Bessel window function with a dk of 3.

Shell-fit analyses of k^3-weighted Fe and As K-edge extended X-ray absorption fine structure (EXAFS) spectra were conducted using the software code Artemis.[29] Theoretical phase-shift and amplitude functions of single and multiple scattering paths were calculated using the ab initio FEFF6 code.[30] The scattering paths used to model the As K-edge EXAFS spectra were extracted from the structure of scorodite ($FeAsO_4{\cdot}2H_2O$)[31] and mansfieldite ($AlAsO_4{\cdot}2H_2O$).[32] For the Fe K-edge EXAFS spectra, we used scorodite, goethite (α-FeOOH),[33] and kaolinite[34] with one Fe substituted for Al in octahedral positions ($Al_3Fe(Si_4O_{10})(OH)_8$) as FEFF input structures. Wavelet transform (WT) analyses of Fe K-edge EXAFS spectra were performed to qualitatively identify the presence of Fe−Si/Al pair correlations in the Kln−Fe(III)−As products, and WT analyses of As K-edge EXAFS spectra were performed to visualize differences in the coordination environment of As in the second coordination shell of Fe(III)−As and Kln−Fe(III)−As products. Here, we used the Fortran-based HAMA code to calculate the WTs.[35] Details of the EXAFS data analyses are provided in Text S4.

RESULTS AND DISCUSSION

Immobilization of As during Fe(II) Oxidation in the Presence and Absence of Kaolinite. The comparison of As concentrations in the ternary Kln&Fe(II)&As and binary Fe(II)&As systems (Figure 1a) showed that the As immobilization during Fe(II) oxidation was significant in the presence of kaolinite but failed in the absence of kaolinite. The

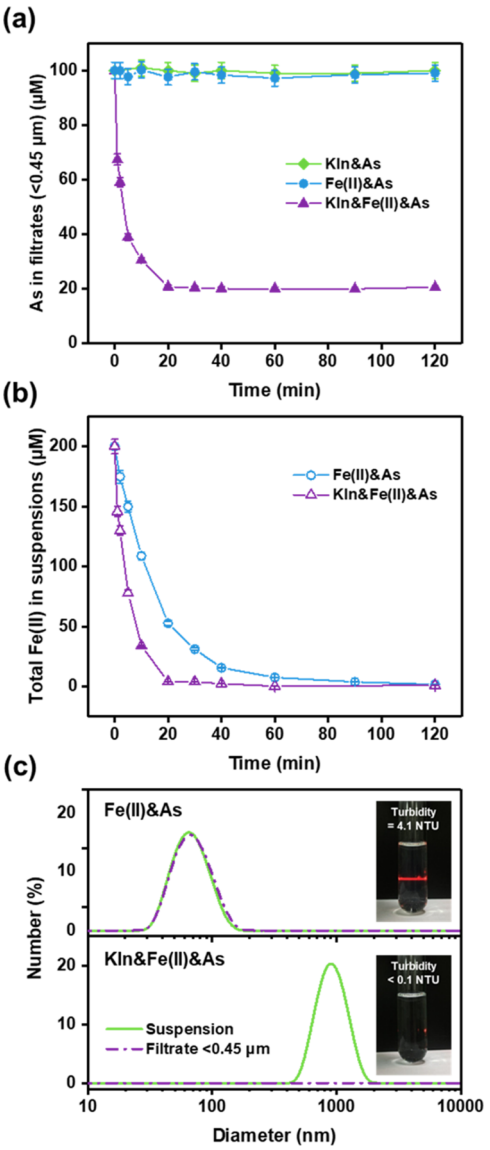

Figure 1. (a) As concentrations in the filtrates (through 0.45 μm filters) of the Kln&As, Fe(II)&As, and Kln&Fe(II)&As systems as a function of oxidation time; (b) total Fe(II) concentrations in the suspensions of the Fe(II)&As and Kln&Fe(II)&As systems as a function of oxidation time; and (c) particle size distribution (PSD), Tyndall effects, and turbidity of the final filtrates and suspensions after 120 min of oxidation in the Fe(II)&As and Kln&Fe(II)&As systems. The initial concentrations of Fe(II), As, and kaolinite (if present) were 200 μM, 100 μM, and 10 g/L, respectively, with a fixed pH of 7.0.

effectiveness of As immobilization was assessed by the decrease of As concentrations passing through a 0.45 μm filter because substances <0.45 μm are usually defined as being "dissolved" and easy to migrate.[36] In the Kln&Fe(II)&As system, As concentrations in the filtrates through 0.45 μm filters rapidly decreased by 80% within 20 min, whereas As concentrations in the filtrates of the Fe(II)&As system were almost unchanged over 120 min of oxidation (Figure 1a). All Fe(II) was oxidized by oxygen after 120 min (Figure 1b). Although it was reported that Fe(II) oxidation could be an effective technique for As removal via coprecipitation of As and Fe(III),[2,4] Fe(II) oxidation in the presence of As or P potentially formed colloidal particles smaller than 0.45 μm that had high

https://doi.org/10.1021/acs.est.4c01976
Environ. Sci. Technol. 2024, 58, 12123−12134

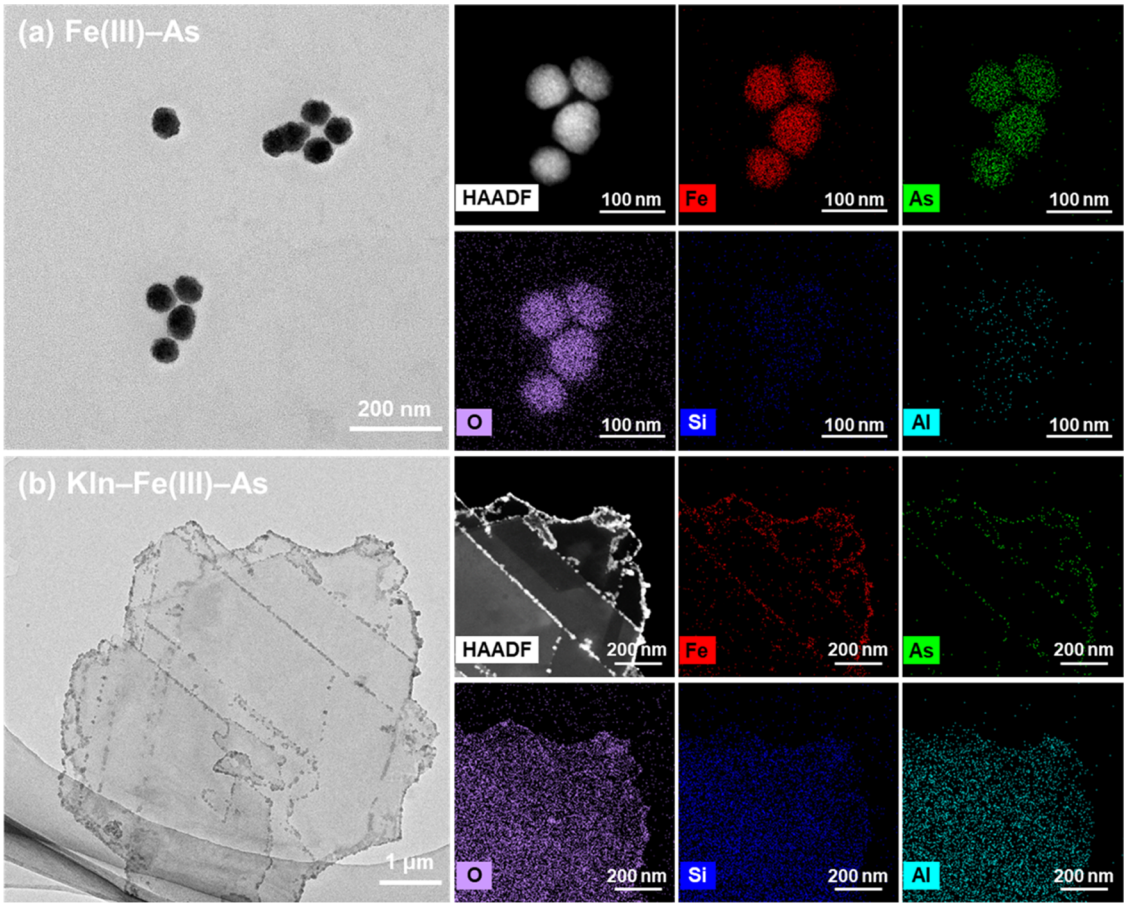

Figure 2. TEM-EDS analyses of (a) Fe(III)−As and (b) Kln−Fe(III)−As products generated from Fe(II) oxidation in the absence and presence of kaolinite. The initial concentrations of Fe(II), As, and kaolinite (if present) were 200 μM, 100 μM, and 10 g/L, respectively, with a fixed pH of 7.0.

mobility.[5,37] Here, the results of particle size distribution, Tyndall effects, and turbidity collectively confirmed the existence of colloidal particles in the filtrates of the Fe(II) &As system (Figure 1c). Such colloids could pass through 0.45 μm filters resulting in no As immobilization in the Fe(II)&As system. In contrast, we observed a clear liquid (without residual solid particles) after filtration by 0.45 μm filters in the Kln&Fe(II)&As system (Figure 1c). We checked the ζ-potentials of pure kaolinite and the oxidation products of Fe(II)&As system, which were −52.3 and −27.6 mV at pH 7.0, respectively. Kaolinite had a more negative surface, so it was incapable of promoting the coagulation of formed colloidal particles. In the Kln&Fe(II)&As system, kaolinite should play a complicated role rather than a coagulant to change the physicochemical characteristics of final As products.

Nanocolloidal Fe(III)−As Formed in the Absence of Kaolinite. According to dynamic light scattering (DLS) and TEM analyses (Figures 1c and 2a), the oxidation products generated in the binary Fe(II)&As system were nanosized particles or aggregates with diameters of 30−200 nm. The TEM image (Figure 2a) showed that single particles were spherical and with ∼50 nm diameters, and several particles aggregated to create a larger aggregate up to 200 nm. The average hydrodynamic diameter was ∼80 nm, as indicated by DLS analysis (Figure 1c). In the high-angle annular dark field (HAADF) image and corresponding element maps (Figure 2a), an aggregate with four spherical particles was clearly observed, and each particle was composed of Fe, As, and O. The element composition was also supported by XPS analysis (Figure S1). The high-resolution XPS spectra for Fe 2p and As 3d as well as the Fe and As K-edge XANES spectra (maxima at 7131.2 eV for Fe and 11874.3 eV for As) verified the valence states of Fe(III) and As(V) (Figures S1 and S2). Such nanocolloidal Fe(III)−As products could completely pass through 0.45 μm filters, resulting in the presence of As in the filtrates (Figure 1a). The monitoring results of Fe(II), Fe(III), and Fe(tot) concentrations in the filtrates (<0.45 μm) proved that all Fe(III) products were transported through the filters (Figure S3). Using 0.02 μm filters to remove the nanocolloidal Fe(III)−As particles from the solution, the truly dissolved As concentrations after Fe(II) oxidation were measured to be 21 μM, and then the molar As/Fe ratio of the Fe(III)−As solid was calculated to be ∼0.40 (i.e., 79/200) in agreement with the value (0.39) obtained from TEM-EDS analyses (Figure S4). Therefore, Fe(II) oxidation transformed truly dissolved As ions only into Fe(III)−As nanocolloids that still had high mobility and environmental risks.

The Fe(III)−As nanocolloids were further characterized by XRD (Figure S5), high-resolution transmission electron microscopy (HRTEM) (Figure S6), and XAS (Figure 3) to reveal their phase composition and structural features. The XRD patterns of Fe(III)−As solids showed no obvious peaks, suggesting to be poorly crystalline (Figure S5). Diffuse spots in the fast Fourier transform (FFT) pattern of the HRTEM image of a single Fe(III)−As nanoparticle also confirmed its poor crystallinity (Figure S6). Carefully, a few lattice fringes

https://doi.org/10.1021/acs.est.4c01976
Environ. Sci. Technol. 2024, 58, 12123−12134

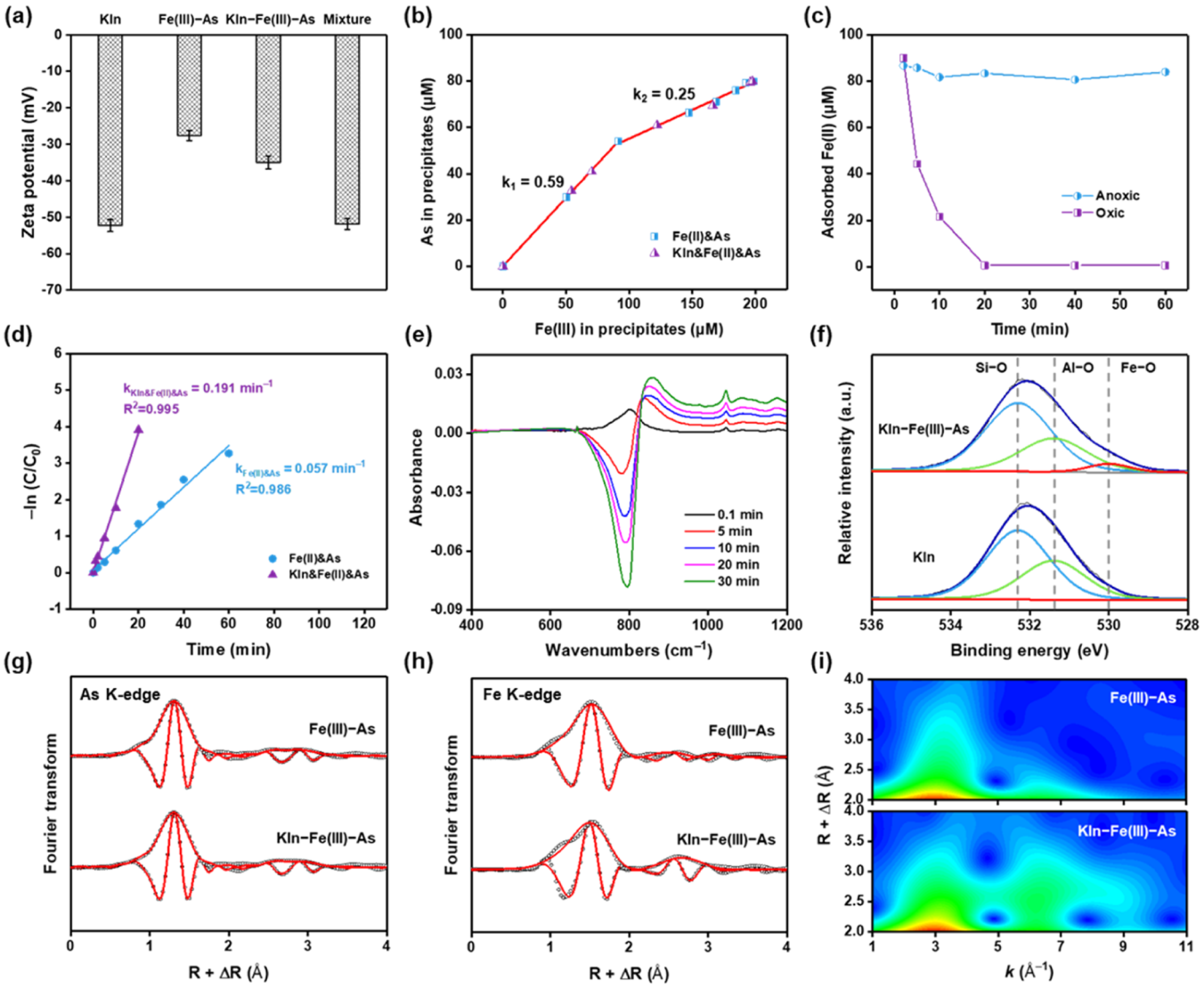

Figure 3. (a) ζ-Potentials of Kln, Fe(III)−As, and Kln−Fe(III)−As and the mixture of Kln and Fe(III)−As; (b) correlation of As and Fe(III) in the Fe(III)−As and Kln−Fe(III)−As precipitates varying with the Fe(II) oxidation extent; (c) adsorbed Fe(II) as a function of reaction time in the Kln&Fe(II)&As system under oxic and anoxic conditions; (d) pseudo-first-order kinetics of total Fe(II) in the Fe(II)&As and Kln&Fe(II)&As systems (based on the raw data in Figure 1b); (e) ATR-FTIR spectra collected during the oxidation of Fe(II) by oxygen on the kaolinite surface in the presence of As; (f) high-resolution XPS spectra of O 1s for Kln−Fe(III)−As and pure kaolinite; (g, h) Fourier-transformed As and Fe K-edge EXAFS spectra of Fe(III)−As and Kln−Fe(III)−As (magnitude and real part (open circles)) and comparison with shell-fits (solid lines, fit parameters in Table 1), and (i) Morlet wavelet transforms of k^2-weighted Fe K-edge EXAFS spectra (κ = 8, σ = 0.8) of Fe(III)−As and Kln−Fe(III)−As.

were observed in the HRTEM image (Figure S6), which had a short-range periodicity of 2.50 Å in agreement with the d-spacing of the ferrihydrite (Fh) (2.55 Å),[38] implying that the Fe(III)−As nanocolloids contain Fh-like short-range-ordered As-rich hydrous ferric oxide (HFO). Previous studies have indicated that the As(V) adsorption maxima of ferrihydrite are about 0.2−0.3 As(V)/Fe,[39,40] which is lower than 0.40 (the As/Fe molar ratio of the Fe(III)−As nanoparticles). This suggested that the As-rich HFO is not the only phase in the Fe(III)−As nanocolloids. Voegelin et al. investigated the Fe(III)−precipitate formation during Fe(II) oxidation in the presence of phosphate at pH 7.0 and concluded that amorphous basic Fe(III)−phosphate with a minimum P/Fe ratio of 0.55 formed first and continuing Fe(II) oxidation resulted in the formation of P-rich HFO.[41] Ehlert et al. also observed a mixture of amorphous Fe(III)−arsenate and As(V)-rich ferrihydrite in the coprecipitates of As(V) and Fe(III) at pH 6.[42] In the HRTEM image, highly disordered and short-range-ordered regions were observed distinctly, which likely displayed the amorphous Fe(III)−arsenate and As-rich HFO (Figure S6). Accordingly, it is reasonable to suggest that the nanocolloidal Fe(III)−As particles are mixtures of different phases (mixing of amorphous basic Fe(III)−arsenate and As-rich HFO within spherical particles).

Arsenic and Fe K-edge EXAFS spectra and their Fourier transforms of the Fe(III)−As nanocolloids confirmed the existence of amorphous basic Fe(III)−arsenate and As-rich HFO (Figures 3g,h and S7). The first-shell-fit of As K-edge EXAFS spectra returned values near 4 for CN_{As-O} and 1.69 Å for R_{As-O} (Table 1), verifying the tetrahedral coordination of As(V).[43] Fit of the second shell was within the fit-derived uncertainties of an As−Fe path with an R_{As-Fe} of 3.29 Å and a

https://doi.org/10.1021/acs.est.4c01976
Environ. Sci. Technol. 2024, 58, 12123−12134

Table 1. EXAFS Parameters Determined by Shell-Fit Analysis of As and Fe K-edge EXAFS Spectra of the Fe(III)−As and Kln−Fe(III)−As Products Generated from Fe(II) Oxidation in the Absence and Presence of Kaolinite[a]

samples	paths	CN[b]	R (Å)[c]	σ^2 (Å^2)[d]	ΔE_0 (eV)[e]	R-factor[f]	red χ^2[g]
			As K-edge EXAFS				
Fe−As	As−O	4.3(0.3)	1.69(0.01)	0.002(0.001)	6.0 (1.0)	0.014	395
	As−O−O	12	3.07(0.01)	0.002(0.001)			
	As−Fe	2.2(0.7)	3.29(0.02)	0.010			
Kln−Fe−As	As−O	4.4(0.3)	1.69(0.01)	0.002(0.001)	5.7(1.0)	0.016	282
	As−O−O	12	3.07(0.01)	0.002(0.001)			
	As−Fe	2.2(0.8)	3.29(0.03)	0.010			
			Fe K-edge EXAFS				
Fe−As	Fe−O	5.6(0.5)	2.00(0.01)	0.008(0.001)	−0.7(0.9)	0.013	426
	Fe−Fe	1.6(0.8)	3.07(0.04)	0.010			
	Fe−As	1.7(0.7)	3.27(0.05)	0.010			
Kln−Fe−As	Fe−O	5.2(0.6)	1.97(0.01)	0.009(0.002)	−1.7(1.4)	0.021	151
	Fe−Fe	1.1(0.5)	3.07(0.04)	0.010			
	Fe−Si	1.2(0.7)	3.23(0.04)	0.010			
	Fe−Al	0.8(0.6)	3.43(0.05)	0.010			

[a]The passive amplitude reduction factor, S_0^2, was fixed as 0.95 (As) or 0.85 (Fe). Fit ranges: $3 \le k \le 13.5$, $0.9 \le R \le 3.6$ for As and $3 \le k \le 11$, $1 \le R \le 4$ for Fe. Parameter uncertainties are given in parentheses. Constrained parameters appear without parentheses. [b]CN is the coordination number (path degeneracy). [c]R is the mean half-path length (interatomic distance). [d]σ^2 is the Debye−Waller parameter. [e]ΔE_0 is the energy shift parameter. [f]R-factor = $\sum_i(\text{data}_i - \text{fit}_i)^2/\sum_i \text{data}_i^2$. [g]Reduced $\chi^2 = N_{idp}/N_{pts} \sum_i((\text{data}_i - \text{fit}_i)/\varepsilon_i)^2/(N_{idp} - N_{var})$, where N_{idp}, N_{pts}, and N_{var}, respectively, are the number of independent points in the model fit, the total number of data points, and the number of variables in the fit, and ε_i is the uncertainty at each data point i.[51]

CN_{As-Fe} of 2.2 (Table 1). These structural parameters were consistent with AsO_4 tetrahedra bonding to Fe(III) polyhedra in the binuclear, corner-sharing geometry,[37] which was also supported by ATR-FTIR analysis showing a strong well-resolved band at 817 cm^{-1} (Figure S8). This kind of local As coordination was previously proposed in amorphous basic Fe(III)−arsenate and As(V)-rich HFO.[44,45]

The shell-fit of Fe K-edge EXAFS spectra yielded an Fe−Fe path with an R_{Fe-Fe} of 3.07 Å and a CN_{Fe-Fe} of 1.6 besides the Fe−As path (Table 1). This Fe−Fe path corresponded to edge-sharing FeO_6,[46] indicating the presence of HFO and basic Fe(III)−arsenate in the Fe(III)−As nanocolloids. For the amorphous Fe(III)−arsenate formed at low pH, Fe−Fe backscattering pairs are absent,[47] but at near-neutral pH, Fe(III) hydrolysis, polymerization, and complexation with arsenate can take place concurrently, resulting in the Fe−Fe linkage in amorphous basic Fe(III)−arsenate.[48] The inclusion of an additional Fe−Fe path with distances of 3.43 Å corresponding to corner-sharing FeO_6 octahedra returned physically impossible CN_{Fe-Fe} values, suggesting that polyhedral linkages of longer distances, such as corner-sharing FeO_6 octahedra, are not present in detectable amounts. The presence of AsO_4 limits the Fe(III) polymerization to the stage of monomers and oligomers, resulting in the formation of Fe(III)−As nanoparticles (as discussed in Text S5).

The uptake capacity of amorphous Fe(III) polymers coprecipitated in the presence of oxyanions has been reported to approach 0.7 mol per mol Fe.[41,45] At the early stage of Fe(II) oxidation, the Fe(III)/As molar ratio in the system is ≪1, which is consistent with the conditions under which amorphous Fe(III)−arsenate forms.[11] The dynamics of the molar As/Fe(III) ratio of the formed Fe(III)−As precipitates confirmed the formation of amorphous basic Fe(III)−arsenate with a molar As/Fe(III) ratio of ∼0.6 at the early stage of Fe(II) oxidation (Figure S10). Moreover, the reduction of As/Fe(III) ratio from about 0.6 to 0.4 over the Fe(II) oxidation time (Figure S10) implied the formation of As-rich HFO in addition to amorphous basic Fe(III)−arsenate. Figure S11 shows the two-stage correlation of As and Fe(III) in the formed Fe(III)−As nanocolloids, which indicates the preferential formation of amorphous basic Fe(III)−arsenate with 0.59 As/Fe(III) and the subsequent formation of As-rich HFO with 0.24 As/Fe(III). Thus, a material consisting of both 46% amorphous basic Fe(III)−arsenate and 54% As-rich HFO can account for the 0.40 As/Fe molar ratio observed in the Fe(III)−As nanocolloids.

Microparticulate Kln−Fe(III)−As Formed in the Presence of Kaolinite. In the presence of kaolinite, micron-sized products with an average hydrodynamic diameter of 0.9 μm were detected (Figure 1c), suggesting that the oxidation products of the Kln&Fe(II)&As system can be easily removed by 0.45 μm filters. The products were mainly composed of O, Si, Al, Fe, and As (Figure S1). Comparing the TEM images of the products and pure kaolinite (Figures 2b and S12), it was found that a new solid phase (dark aggregates in the bright-field TEM image) emerged at the edges of the kaolinite plates. Element maps showed that the outer ring of kaolinite plates was composed of Fe and As (Figure 2b), indicating newly formed Fe−As phases on the edge surfaces of kaolinite. This kind of distribution of oxidation products was unlike that in a Mn(II)&Kln system reported by Yang et al.[49] They found that the crystallization of MnO_x mostly occurred on the basal surfaces of kaolinite after 28 days of reaction. The different phenomena may be related to the limited loading capacity of the edge surfaces of kaolinite as well as the surface charge of the newly formed phases. The loading amount of metal on kaolinite surfaces in the Mn(II)&Kln system (400 μmol Mn per g kaolinite) was much higher than that in our Fe(II)&Kln system (20 μmol Fe per g kaolinite), so that only <5% of initial aqueous Mn(II) were adsorbed by the edge surfaces of kaolinite.[49] As a result, most of the Mn(II) oxidation and further precipitation might occur outside the edge surfaces. Moreover, the newly formed MnO_x had positively charged surfaces and could be electrostatically attracted by the

https://doi.org/10.1021/acs.est.4c01976
Environ. Sci. Technol. 2024, 58, 12123−12134

negatively charged basal surfaces of kaolinite, resulting in their further crystallization by particle attachment on the basal surfaces.[49] For our Fe(II)&Kln system with As(V), however, the crystallization of Fe−As phases on the basal surfaces should be hindered due to the negatively charged surfaces of Fe−As phases (Figure 3a). Thus, we believe that the edge surfaces of kaolinite are dominant in hosting Fe−As phases due to their higher reactivity than basal surfaces.[16,50]

The molar As/Fe(III) ratio of the Kln−Fe(III)−As product was 0.4 (i.e., 80/200) consistent with that of Fe(III)−As precipitates generated in the kaolinite-free system, implying the similarity of newly formed Fe(III)−As phases in the presence and absence of kaolinite. In the edge region of the Kln−Fe(III)−As product, two solid phases with a clear boundary were observed in the enlarged TEM image (Figure S13), which were kaolinite and Fe(III)−As phases, respectively. The HRTEM image of the Fe(III)−As phases showed disordered regions as well as a few short-range-ordered nanocrystals (Figure S13), indicating the presence of two types of possible Fe(III)−As phases. The short-range-ordered nanocrystals had a d-spacing of 2.50 Å (Figure S13) in agreement with the short-range-ordered HFO in the Fe(III)−As nanocolloids (Figure S6). And the disordered region may be amorphous basic Fe(III)−arsenate as that in the Fe(III)−As nanocolloids. The monitoring of the As/Fe(III) molar ratio of newly formed precipitates on kaolinite surfaces supported the presence of amorphous basic Fe(III)−arsenate that has a molar As/Fe(III) ratio of ∼0.6 (Figure S10), similar to that in the kaolinite-free system. The reduction of As/Fe(III) ratios to 0.4 came earlier than that of the kaolinite-free system (Figure S10). These similar features in the morphology and composition of Fe(III)−As phases formed in the presence and absence of kaolinite indicated that Fe(III)−As phases on kaolinite surfaces were also mixtures of amorphous basic Fe(III)−arsenate and As-rich HFO, whose As/Fe(III) ratios were 0.59 and 0.25 (Figure 3b), respectively.

The similar As K-edge EXAFS spectra of Fe(III)−As and Kln−Fe(III)−As products confirmed their similar As local coordination (Figures S7 and 3g). Shell-fit of the As K-edge EXAFS spectrum of Kln−Fe(III)−As returned an As−Fe path with an R_{As-Fe} of 3.29 Å and a CN_{As-Fe} of 2.2 (Table 1), which was identical to the results for Fe(III)−As nanocolloids in the kaolinite-free system. This identity is further visualized in Figure S14, where the wavelet transform plots showed the same signal intensity of backscattering As in the Fe(III)−As and Kln−Fe(III)−As products. Therefore, we further conclude that As phases in the Kln−Fe(III)−As product include amorphous basic Fe(III)−arsenate and As(V)-rich HFO (with mainly edge-sharing Fe(III)-polymers) as that in the Fe(III)−As nanocolloids, maybe via heterogeneous precipitation on kaolinite surfaces.

Role of Kaolinite in As Immobilization during Fe(II) Oxidation. The possibilities of (i) adsorption or coadsorption of As onto kaolinite and (ii) deposition of Fe(III)−As nanocolloids on kaolinite were excluded (as shown in Text S6). Therefore, kaolinite most likely participated in As immobilization in the ternary Kln&Fe(II)&As system from beginning to end. The possible processes may include Fe(II) adsorption onto kaolinite, heterogeneous Fe(II) oxidation, and heterogeneous coprecipitation of Fe(III) and As on kaolinite surfaces.

Fe(II) Adsorption onto Kaolinite. A dynamic process of Fe(II) adsorption in the Kln&Fe(II)&As system during Fe(II) oxidation is shown in Figure 3c, which was determined by the difference of Fe(II) concentrations in suspensions and filtrates. The amounts of adsorbed Fe(II) at pH 7.0 gradually decreased with Fe(II) oxidation. The initial adsorbed Fe(II) was ascribed to the rapid adsorption of Fe(II) by kaolinite, which occurred within several seconds as dissolved Fe(II) encountered kaolinite (Figure 3c). According to the adsorption isotherm experiments under anoxic conditions (Figure S16), the maximal adsorption capacity of Fe(II) onto kaolinite was ∼11.7 μmol/g at pH 7.0, which was derived from the Langmuir isotherm model, showing the significant adsorption ability of kaolinite for Fe(II). The negatively charged surface of kaolinite provided favorable conditions for Fe(II) adsorption, and the ζ-potential at pH 7.0 was −52.3 mV (Figure 3a). The surface negative charge of kaolinite at neutral pH mainly comes from pH-dependent variable charge caused by deprotonation of hydroxyl groups on edge surfaces (e.g., ≡Si−OH and ≡Al−OH), while that resulted from basal sites is few due to the limited structural substitution.[16] At pH values below 8.0, Fe(II) is present as positively charged Fe^{2+} cations (Figure S15), resulting in the natural attraction between kaolinite and Fe(II). Although both inner-sphere surface complexation on the edge sites and cation exchange on the basal sites could lead to Fe(II) adsorption, the former was dominant since the basal sites on kaolinite were commonly less than 10%.[50,52]

According to the *in situ* ATR-FTIR analysis, a negative peak at 780−795 cm^{-1} appeared and increased with the ongoing Fe(II) oxidation (Figure 3e), which could be assigned to decreasing intensities of the Al−O−Si bending vibration in kaolinite.[53] The attenuated Al−O−Si bending vibration indicated that the ≡Al−O−Si≡ sites contributed to Fe(II) adsorption. Moreover, the shell-fit of the Fe K-edge EXAFS spectrum for the Kln−Fe(III)−As product returned an Fe−Al path with an R_{Fe-Al} of 3.43 Å (Table 1), indicating that one orientation for the formed inner-sphere complexes is bidentate bonding of Fe to oxygen atoms at two ≡Al−O−Si≡ edge sites or one ≡Al−O−Si≡ and one ≡Al−OH edge sites.[54] An Fe−Si path with an R_{Fe-Si} of 3.23 Å was also obtained (Table 1), which corresponded to the monodentate bonding of Fe to ≡Si−OH edge sites.[55] In consequence, the active sites on the kaolinite surfaces included ≡Al−O−Si≡, ≡Al−OH, and ≡Si−OH edge sites, consistent with previous theoretical simulations and experimental results.[56,57]

In addition, the newly formed Fe(III) precipitates on kaolinite surfaces due to the heterogeneous oxidation of adsorbed Fe(II) could also contribute to further Fe(II) adsorption. The role of Fe(III) precipitates in Fe(II) adsorption during Fe(II) oxidation has been widely considered to be an important player in transforming homogeneous oxidation to heterogeneous oxidation in a pure Fe(II) solution.[28] Although kaolinite was not the only adsorbent for Fe(II), it was responsible for the early Fe(II) adsorption and provided a platform for the accumulation of Fe(III) solid phases, implying that the subsequent reactions associated with As immobilization would also be related to kaolinite.

Heterogeneous Fe(II) Oxidation. The accelerated oxidation of Fe(II) in the Kln&Fe(II)&As system compared to that in the Fe(II)&As system (Figure 1b) was caused by the heterogeneous Fe(II) oxidation on kaolinite surfaces. According to Figure 3d, the Fe(II) oxidation in both Kln&Fe(II)&As and Fe(II)&As systems followed pseudo-first-order kinetics. The rate constants for Fe(II) oxidation in the Kln&Fe(II)&As and Fe(II)&As systems were 0.191 and 0.057 min^{-1},

https://doi.org/10.1021/acs.est.4c01976
Environ. Sci. Technol. 2024, 58, 12123−12134

Scheme 1. Heterogeneous Pathway of As(V) Immobilization on Kaolinite Edge Surfaces Driven by Fe(II) Oxidation

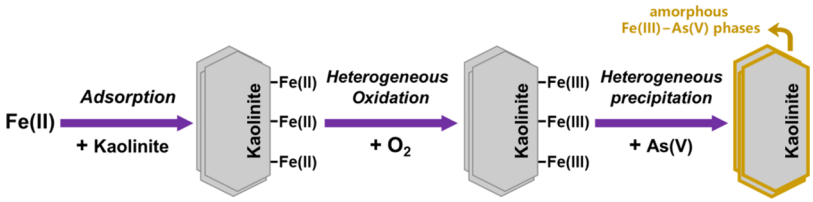

respectively, indicating that the Fe(II) oxidation rate of the Kln&Fe(II)&As system was approximately 3.4 times that of the Fe(II)&As system. The enhanced Fe(II) oxidation is related to the inner-sphere complexation of Fe(II) on surface oxygen/hydroxyl sites of kaolinite.[27] This kind of complexation can alter the coordination environment around the Fe(II) center and thereby make adsorbed Fe(II) a better reducing agent.[26] It is necessary to point out that the kaolinite-induced heterogeneous Fe(II) oxidation predominated only in the initial stage of Fe(II) oxidation. When Fe(III) solid phases resulting from Fe(II) oxidation accumulated and covered kaolinite surfaces, Fe(II) adsorption on Fe(III) solid phases primarily occurred, which began to dominate the subsequent heterogeneous Fe(II) oxidation until all Fe(II) was transformed to Fe(III).

Heterogeneous Nucleation and Precipitation of Fe(III)−As Phases. The formation of Fe(III)−As phases, including amorphous basic Fe(III)−arsenate and As-rich HFO in the Kln−Fe(III)−As product, should involve the heterogeneous nucleation and precipitation of Fe(III) and As on the surface of kaolinite. Two possible heterogeneous nucleation pathways were supposed: (i) a synchronous pathway for amorphous basic Fe(III)−arsenate, where Fe(III) and arsenate ions nucleated simultaneously on kaolinite surfaces, forming amorphous basic Fe(III)−arsenate directly; (ii) a stepwise pathway for As-rich HFO, where HFO formed first on kaolinite edges and was transformed subsequently to As-rich HFO upon reacting with As. In either case, the interaction between Fe(III) and kaolinite edge sites was essential for heterogeneous nucleation and precipitation.

Iron K-edge EXAFS and ATR-FTIR analyses confirmed the interaction between Fe and kaolinite. The fitted Fe−Al path with an R_{Fe-Al} of 3.43 Å from the Fe K-edge EXAFS spectrum (Table 1) and the negative peak at 780−795 cm^{-1} in the ATR-FTIR spectrum (Figure 3e) together highlighted the role of ≡Al−O−Si≡ sites in bonding Fe. Other active sites included ≡Al−OH and ≡Si−OH edge sites based on the Fe K-edge EXAFS analysis (Table 1). The presence of Fe−Si/Al near-neighbor pair interaction was also illustrated in the corresponding wavelet transform of the Fe K-edge EXAFS spectrum of the Kln−Fe(III)−As product, in which a new scattering signal at $R + \Delta R$ = 2.6 Å and k = 6.3 $Å^{-1}$ occurred relative to that in the Fe(III)−As product (Figure 3i).

According to the *in situ* ATR-FTIR analysis, the attenuation at 780−795 cm^{-1} (corresponding to the bending vibration of Al−O−Si) and growth at 840−860 cm^{-1} (due to the stretching vibration of As−O) (Figure 3e) occurred simultaneously,[53,58] implying that the complexation of Fe to ≡Al−O−Si≡ sites and the linkage of Fe and As were simultaneous. This process may result in the formation of amorphous basic Fe(III)−arsenate via the simultaneous nucleation of Fe(III) and As on kaolinite surfaces.

The formation of As-rich HFO on kaolinite surfaces was evidenced collectively by Fe K-edge EXAFS, ATR-FTIR, and XPS analyses. Shell-fit of the Fe K-edge EXAFS spectrum of the Kln−Fe(III)−As product yielded an Fe−Fe path with an R_{Fe-Fe} of 3.07 Å (Table 1) attributed to edge-sharing FeO_6, indicating the presence of HFO in the Kln−Fe(III)−As product.[46] According to the *in situ* ATR-FTIR analysis of Fe(II) oxidation in the presence of kaolinite and As, the peak at 1047 cm^{-1} due to the bending vibration of hydroxyl groups of Fe−OH gradually increased (Figure 3e), suggesting the formation of HFO on kaolinite surfaces.[8] This newly formed HFO was also supported by the high-resolution XPS spectrum of O 1s of the Kln−Fe(III)−As product, in which a new peak at 530.0 eV analogous to lattice oxygen O^{2-} in Fe(III) (hydr)oxides was observed.[59]

In summary, As(V) was immobilized via a three-step heterogeneous pathway in the presence of kaolinite driven by Fe(II) oxidation (Scheme 1). First, kaolinite rapidly adsorbed Fe(II) onto its surface sites at the mineral edge via forming inner-sphere complexes within several seconds, including monodentate mononuclear complexes corner-sharing with ≡Si−OH sites and bidentate binuclear complexes corner-sharing with ≡Al−O−Si≡ oxygen sites and ≡Al−OH hydroxyl sites. This kind of complexation allowed adsorbed Fe(II) to be oxidized in a heterogeneous way, with a significantly enhanced rate relative to homogeneous oxidation. After Fe(II) oxidation, the newly formed Fe(III) would heterogeneously nucleate and precipitate with As on kaolinite surfaces. In the end, the dissolved As was immobilized as micron-sized Kln−Fe(III)−As ternary precipitates, thereby limiting As mobility.

Environmental Implications. We report that kaolinite enhances As(V) immobilization during Fe(II) oxidation by inducing the formation of As-bearing products with large sizes to reduce the As mobility. Kaolinite surfaces provide edge sites for Fe(II) adsorption, subsequent heterogeneous oxidation, and the final heterogeneous nucleation and precipitation of Fe(III)−As phases surrounding the edge. In contrast to the prior notion that the fate of As was almost not affected by kaolinite,[13] this work highlights the significant role of kaolinite in As immobilization. The presence of kaolinite suppresses the formation of Fe(III)−As nanocolloids regardless of DO concentrations and pH (Figure S18), which may be of particular significance to adequate prediction and assessment of As transport in subsurface environments.

The interaction between kaolinite and As with Fe as a bridge characterized here also offers a new perspective to understand the impact of other nonferrous minerals in subsurface environments on the fate of As as well as other oxyanions like phosphate. In this work, we reveal that the impact of kaolinite on As species transformation is based on its role in catalyzing Fe(II) oxidation and in forming associations with the resulting Fe(III) phases. Considering the reported role of montmorillonite, illite, AlOOH, Al_2O_3, and TiO_2 in catalyzing

https://doi.org/10.1021/acs.est.4c01976
Environ. Sci. Technol. 2024, 58, 12123−12134

Fe(II) oxidation via surface adsorption,[60−63] we believe that these nonferrous minerals may have similar impacts on As species transformation.

The role of kaolinite in suppressing the Fe(III)−As nanocolloid formation can be expected for anoxic groundwater containing Fe(II) and arsenate when brought into contact with O_2, for example, by the introduction of DO due to groundwater table fluctuation.[24] Considering the flow characteristics of groundwater and the dynamics of Fe(II) oxidation,[41,64] spatially separated formation of Fe(III)−As nanocolloids may develop along subsurface flow paths. Also, partial Fe(II) oxidation due to limited dissolved oxygen may result in the localized formation of Fe(III)−As nanocolloids, even in waters with high Fe(II)/As ratios. In both cases, the presence of kaolinite can lead to the formation of large-sized Kln−Fe(III)−As precipitates rather than Fe(III)−As nanocolloids, reducing As mobility. Moreover, the shift of Fe(III)−As nanocolloids to Kln−Fe(III)−As precipitates is applicable to low DO conditions (Figure S18), suggesting that the role of kaolinite in controlling As species has extensive environmental significance.

This study focused on the effect of kaolinite at a relatively low initial Fe(II)/As ratio until complete Fe(II) oxidation, avoiding the masking effects of large-sized products formed at high initial Fe/As ratios on kaolinite's roles. Figure S18 shows that the formation of Fe(III)−As nanocolloids was usual at initial Fe(II)/As molar ratios ≤2, while large-sized products that can be retained by 0.45 μm filters were formed dominantly at high Fe(II)/As initial ratios due to the precipitation of different Fe(III) phases and the reduced negative surface charge.[6,65] As a result, the role of kaolinite in As immobilization should be concealed at high initial Fe(II)/As ratios, although the heterogeneous precipitation of Fe(III)−As phases on kaolinite surfaces still occurred. Relatively low initial Fe/As ratios are frequent in high-As-contaminated groundwater of industrial sites. In this study, the As concentration used was at a mg/L level, consistent with As-contaminated groundwater reported in mining, smelters, and chemical industry-related sites.[66,67]

Although we have investigated several factors, including kaolinite concentrations, DO concentrations, pH, and initial Fe/As ratios (Figure S18), there are still many other factors that might interfere with the interaction among Fe, As, and kaolinite in the real natural environment, such as other minerals, organic matter, and other cations and oxyanions. The presence of metal oxides with strong affinity for As may lead to the direct adsorption of As on mineral surfaces,[68] competing with the uptake of As by newly formed Fe(III)-phases from Fe(II) oxidation in bulk solution and/or on kaolinite surfaces. When permanent charge-rich clay minerals like smectite coexist with kaolinite, part of As may be immobilized on basal surfaces of permanent charge-rich clay minerals via forming cation bridging complexes of As.[19] Organic matter (OM), such as humic substances, has abundant functional groups that can participate in the reaction among kaolinite, Fe, and As to form various possible products like OM−Fe−As and Kln−OM−Fe−As.[10] In the presence of competing cations with Fe(II), especially those having a stronger affinity to kaolinite edge sites (e.g., Cu and Pb),[16] less Fe(II) could be adsorbed and oxidized on the surface of kaolinite and thus less Kln−Fe(III)−As precipitates could be generated. Also, the presence of competing oxyanions with As could impact the formation of Fe(III)−As precipitates as well as ternary Kln−Fe(III)−As precipitates by occupying available Fe(III) sites.[4] Therefore, further studies are required to quantify the effects of coexisting components in the real natural environment on Fe oxidation, precipitation, and the resulting impact on As transformation in the presence of kaolinite.

■ ASSOCIATED CONTENT

Supporting Information

The Supporting Information is available free of charge at https://pubs.acs.org/doi/10.1021/acs.est.4c01976.

Materials and chemicals; Fe(II) adsorption experiments and results under anoxic conditions; details of the ATR-FTIR method; details of the XAS data analysis; additional discussion on the formation of nanocolloidal Fe(III)−As particles; discussion on the possibility of As adsorption/coadsorption on kaolinite and deposition of Fe(III)−As nanocolloids on kaolinite; results and discussion on the impacts of various factors; XPS, XAS, XRD, TEM, ATR-FTIR, and in situ DLS analyses of the products from different systems; dynamic variation of Fe(II), Fe(III), and Fe(tot) concentrations in filtrates and molar As/Fe(III) ratios in precipitates over the Fe(II) oxidation time; and effect of kaolinite on the stability of the Fe(III)−As nanocolloid suspension (PDF)

■ AUTHOR INFORMATION

Corresponding Authors

Shengyan Pu − *State Key Laboratory of Geohazard Prevention and Geoenvironment Protection, College of Ecology and Environment, Chengdu University of Technology, Chengdu 610059, China;* orcid.org/0000-0003-1610-1589; Email: pushengyan13@cdut.edu.cn

Linling Wang − *School of Environmental Science and Engineering, Huazhong University of Science and Technology, Wuhan 430074, China;* orcid.org/0000-0001-7468-9064; Email: wanglinling@hust.edu.cn

Authors

Xin Wang − *State Key Laboratory of Geohazard Prevention and Geoenvironment Protection, College of Ecology and Environment, Chengdu University of Technology, Chengdu 610059, China; School of Environmental Science and Engineering, Huazhong University of Science and Technology, Wuhan 430074, China;* orcid.org/0000-0001-6379-9436

Jiaqi Ding − *School of Environmental Science and Engineering, Huazhong University of Science and Technology, Wuhan 430074, China*

Jing Chen − *School of Environmental Science and Engineering, Huazhong University of Science and Technology, Wuhan 430074, China;* orcid.org/0000-0002-7243-0806

Peng Liao − *State Key Laboratory of Environmental Geochemistry, Institute of Geochemistry, Chinese Academy of Sciences, Guiyang 550081, China;* orcid.org/0000-0001-6924-1097

Delai Zhong − *Key Laboratory of the Three Gorges Reservoir Region's Eco-Environment, Ministry of Education, College of Environment and Ecology, Chongqing University, Chongqing 400044, China;* orcid.org/0000-0003-1394-8346

Daniel C. W. Tsang − *Department of Civil and Environmental Engineering, The Hong Kong University of*

https://doi.org/10.1021/acs.est.4c01976
Environ. Sci. Technol. 2024, 58, 12123−12134

Science and Technology, Hong Kong, China; orcid.org/0000-0002-6850-733X

John C. Crittenden − *School of Environmental Science and Engineering, Huazhong University of Science and Technology, Wuhan 430074, China; Brook Byers Institute for Sustainable Systems, School of Civil and Environmental Engineering, Georgia Institute of Technology, Atlanta, Georgia 30332, United States*

Complete contact information is available at: https://pubs.acs.org/10.1021/acs.est.4c01976

Notes

The authors declare no competing financial interest.

■ ACKNOWLEDGMENTS

This work was supported by the National Natural Science Foundation of China (Nos. 42207307, 22076053, and U22A20591), the National Key Research and Development Program of China (No. 2020YFC1808300), the Opening Fund of State Key Laboratory of Geohazard Prevention and Geoenvironment Protection (Chengdu University of Technology) (No. SKLGP2023K026), and the China Scholarship Council (No. 202308510313). The authors would like to thank the Analytical and Testing Center at Huazhong University of Science and Technology, the State Key Laboratory of Pollution Control and Resource Reuse at Tongji University, and the Beijing Synchrotron Radiation Facility for their assistance with sample characterization. The authors also appreciate the support from the Brook Byers Institute for Sustainable Systems, Hightower Chair, and Georgia Research Alliance at the Georgia Institute of Technology. The views and ideas expressed herein are solely those of the authors and do not represent the ideas of the funding agencies in any form.

■ REFERENCES

(1) Wallis, I.; Prommer, H.; Berg, M.; Siade, A. J.; Sun, J.; Kipfer, R. The river−groundwater interface as a hotspot for arsenic release. *Nat. Geosci.* **2020**, *13* (4), 288−295.

(2) Roberts, L. C.; Hug, S. J.; Ruettimann, T.; Billah, M. M.; Khan, A. W.; Rahman, M. T. Arsenic removal with iron(II) and iron(III) in waters with high silicate and phosphate concentrations. *Environ. Sci. Technol.* **2004**, *38* (1), 307−315.

(3) Ouyang, L.; Song, F.; Yu, C.; Huang, L.; Shuai, Q. Efficient arsenic coagulation by serpentine-mediated iron hydroxides. *Chem. Commun.* **2023**, *59* (42), 6410−6413.

(4) Senn, A.-C.; Hug, S. J.; Kaegi, R.; Hering, J. G.; Voegelin, A. Arsenate co-precipitation with Fe(II) oxidation products and retention or release during precipitate aging. *Water Res.* **2018**, *131*, 334−345.

(5) van Genuchten, C. M.; Peña, J.; Amrose, S. E.; Gadgil, A. J. Structure of Fe(III) precipitates generated by the electrolytic dissolution of Fe(0) in the presence of groundwater ions. *Geochim. Cosmochim. Acta* **2014**, *127*, 285−304.

(6) Ahmad, A.; van Genuchten, C. M. Deep-dive into iron-based co-precipitation of arsenic: A review of mechanisms derived from synchrotron techniques and implications for groundwater treatment. *Water Res.* **2024**, *249*, No. 120970.

(7) Kretzschmar, R.; Schäfer, T. Metal retention and transport on colloidal particles in the environment. *Elements* **2005**, *1* (4), 205−210.

(8) Sharma, P.; Ofner, J.; Kappler, A. Formation of binary and ternary colloids and dissolved complexes of organic matter, Fe and As. *Environ. Sci. Technol.* **2010**, *44* (12), 4479−4485.

(9) Sharma, P.; Rolle, M.; Kocar, B.; Fendorf, S.; Kappler, A. Influence of natural organic matter on As transport and retention. *Environ. Sci. Technol.* **2011**, *45* (2), 546−553.

(10) Sundman, A.; Karlsson, T.; Sjöberg, S.; Persson, P. Complexation and precipitation reactions in the ternary As(V)−Fe(III)−OM (organic matter) system. *Geochim. Cosmochim. Acta* **2014**, *145*, 297−314.

(11) van Genuchten, C. M.; Gadgil, A. J.; Peña, J. Fe(III) nucleation in the presence of bivalent cations and oxyanions leads to subnanoscale 7 Å polymers. *Environ. Sci. Technol.* **2014**, *48* (20), 11828−11836.

(12) Liu, X.; Tournassat, C.; Grangeon, S.; Kalinichev, A. G.; Takahashi, Y.; Marques Fernandes, M. Molecular-level understanding of metal ion retention in clay-rich materials. *Nat. Rev. Earth Environ.* **2022**, *3* (7), 461−476.

(13) Uddin, M. K. A review on the adsorption of heavy metals by clay minerals, with special focus on the past decade. *Chem. Eng. J.* **2017**, *308*, 438−462.

(14) Bhattacharyya, K. G.; Gupta, S. S. Adsorption of a few heavy metals on natural and modified kaolinite and montmorillonite: A review. *Adv. Colloid Interface Sci.* **2008**, *140* (2), 114−131.

(15) Soltermann, D.; Marques Fernandes, M.; Baeyens, B.; Miehé-Brendlé, J.; Dähn, R. Competitive Fe(II)−Zn(II) uptake on a synthetic montmorillonite. *Environ. Sci. Technol.* **2014**, *48* (1), 190−198.

(16) Gu, X.; Evans, L. J. Surface complexation modelling of Cd(II), Cu(II), Ni(II), Pb(II) and Zn(II) adsorption onto kaolinite. *Geochim. Cosmochim. Acta* **2008**, *72* (2), 267−276.

(17) Bentahar, Y.; Hurel, C.; Draoui, K.; Khairoun, S.; Marmier, N. Adsorptive properties of Moroccan clays for the removal of arsenic(V) from aqueous solution. *Appl. Clay Sci.* **2016**, *119*, 385−392.

(18) Martin, M.; Violante, A.; Ajmone-Marsan, F.; Barberis, E. Surface interactions of arsenite and arsenate on soil colloids. *Soil Sci. Soc. Am. J.* **2014**, *78* (1), 157−170.

(19) Fakhreddine, S.; Fendorf, S. The effect of porewater ionic composition on arsenate adsorption to clay minerals. *Sci. Total Environ.* **2021**, *785*, No. 147096.

(20) Huang, J.; Jones, A.; Waite, T. D.; Chen, Y.; Huang, X.; Rosso, K. M.; Kappler, A.; Mansor, M.; Tratnyek, P. G.; Zhang, H. Fe(II) redox chemistry in the environment. *Chem. Rev.* **2021**, *121* (13), 8161−8233.

(21) Shi, Q.; Sterbinsky, G. E.; Zhang, S.; Christodoulatos, C.; Korfiatis, G. P.; Meng, X. Formation of Fe(III)−As(V) complexes: Effect on the solubility of ferric hydroxide precipitates and molecular structural identification. *Environ. Sci. Nano* **2020**, *7* (5), 1388−1398.

(22) Kleber, M.; Bourg, I. C.; Coward, E. K.; Hansel, C. M.; Myneni, S. C. B.; Nunan, N. Dynamic interactions at the mineral−organic matter interface. *Nat. Rev. Earth Environ.* **2021**, *2* (6), 402−421.

(23) Ito, A.; Wagai, R. Global distribution of clay-size minerals on land surface for biogeochemical and climatological studies. *Sci. Data* **2017**, *4* (1), No. 170103.

(24) Wei, Y.; Chen, Y.; Cao, X.; Xiang, M.; Huang, Y.; Li, H. A critical review of groundwater table fluctuation: Formation, effects on multifields, and contaminant behaviors in a soil and aquifer system. *Environ. Sci. Technol.* **2024**, *58* (5), 2185−2203.

(25) Zhang, P.; Yao, W.; Yuan, S. Citrate-enhanced release of arsenic during pyrite oxidation at circumneutral conditions. *Water Res.* **2017**, *109*, 245−252.

(26) Jones, A. M.; Griffin, P. J.; Collins, R. N.; Waite, T. D. Ferrous iron oxidation under acidic conditions—The effect of ferric oxide surfaces. *Geochim. Cosmochim. Acta* **2014**, *145*, 1−12.

(27) Chen, C.; Thompson, A. Ferrous iron oxidation under varying pO_2 levels: The effect of Fe(III)/Al(III) oxide minerals and organic matter. *Environ. Sci. Technol.* **2018**, *52* (2), 597−606.

(28) Kinsela, A. S.; Jones, A. M.; Bligh, M. W.; Pham, A. N.; Collins, R. N.; Harrison, J. J.; Wilsher, K. L.; Payne, T. E.; Waite, T. D. Influence of dissolved silicate on rates of Fe(II) oxidation. *Environ. Sci. Technol.* **2016**, *50* (21), 11663−11671.

(29) Ravel, B.; Newville, M. ATHENA, ARTEMIS, HEPHAESTUS: data analysis for X-ray absorption spectroscopy using IFEFFIT. *J. Synchrotron Radiat.* **2005**, *12* (4), 537−541.

(30) Zabinsky, S. I.; Rehr, J. J.; Ankudinov, A.; Albers, R. C.; Eller, M. J. Multiple-scattering calculations of X-ray-absorption spectra. *Phys. Rev. B* **1995**, *52* (4), 2995−3009.
(31) Kitahama, K.; Kiriyama, R.; Baba, Y. Refinement of the crystal structure of scorodite. *Acta Crystallogr., Sect. B: Struct. Sci.* **1975**, *31* (1), 322−324.
(32) Harrison, W. T. A. Synthetic mansfieldite, $AlAsO_4{\cdot}2H_2O$. *Acta Crystallogr., Sect. C: Cryst. Struct. Commun.* **2000**, *56* (10), No. e421.
(33) Gualtieri, A. F.; Venturelli, P. In situ study of the goethite-hematite phase transformation by real time synchrotron powder diffraction. *Am. Mineral.* **1999**, *84* (5−6), 895−904.
(34) Bish, D. L.; Von Dreele, R. B. Rietveld refinement of non-hydrogen atomic positions in kaolinite. *Clays Clay Miner.* **1989**, *37* (4), 289−296.
(35) Funke, H.; Scheinost, A. C.; Chukalina, M. Wavelet analysis of extended X-ray absorption fine structure data. *Phys. Rev. B* **2005**, *71* (9), No. 094110.
(36) Aiken, G. R.; Hsu-Kim, H.; Ryan, J. N. Influence of dissolved organic matter on the environmental fate of metals, nanoparticles, and colloids. *Environ. Sci. Technol.* **2011**, *45* (8), 3196−3201.
(37) van Genuchten, C. M.; Addy, S. E. A.; Peña, J.; Gadgil, A. J. Removing arsenic from synthetic groundwater with iron electrocoagulation: An Fe and As K-Edge EXAFS study. *Environ. Sci. Technol.* **2012**, *46* (2), 986−994.
(38) Voegelin, A.; Kaegi, R.; Frommer, J.; Vantelon, D.; Hug, S. J. Effect of phosphate, silicate, and Ca on Fe(III)-precipitates formed in aerated Fe(II)- and As(III)-containing water studied by X-ray absorption spectroscopy. *Geochim. Cosmochim. Acta* **2010**, *74* (1), 164−186.
(39) Dixit, S.; Hering, J. G. Comparison of arsenic(V) and arsenic(III) sorption onto iron oxide minerals: Implications for arsenic mobility. *Environ. Sci. Technol.* **2003**, *37* (18), 4182−4189.
(40) Fuller, C. C.; Davis, J. A.; Waychunas, G. A. Surface chemistry of ferrihydrite: Part 2. Kinetics of arsenate adsorption and coprecipitation. *Geochim. Cosmochim. Acta* **1993**, *57* (10), 2271−2282.
(41) Voegelin, A.; Senn, A.-C.; Kaegi, R.; Hug, S. J.; Mangold, S. Dynamic Fe-precipitate formation induced by Fe(II) oxidation in aerated phosphate-containing water. *Geochim. Cosmochim. Acta* **2013**, *117*, 216−231.
(42) Ehlert, K.; Mikutta, C.; Jin, Y.; Kretzschmar, R. Mineralogical controls on the bioaccessibility of arsenic in Fe(III)−As(V) coprecipitates. *Environ. Sci. Technol.* **2018**, *52* (2), 616−627.
(43) Adra, A.; Morin, G.; Ona-Nguema, G.; Brest, J. Arsenate and arsenite adsorption onto Al-containing ferrihydrites. Implications for arsenic immobilization after neutralization of acid mine drainage. *Appl. Geochem.* **2016**, *64*, 2−9.
(44) Chen, N.; Jiang, D. T.; Cutler, J.; Kotzer, T.; Jia, Y. F.; Demopoulos, G. P.; Rowson, J. W. Structural characterization of poorly-crystalline scorodite, iron(III)−arsenate co-precipitates and uranium mill neutralized raffinate solids using X-ray absorption fine structure spectroscopy. *Geochim. Cosmochim. Acta* **2009**, *73* (11), 3260−3276.
(45) Waychunas, G. A.; Rea, B. A.; Fuller, C. C.; Davis, J. A. Surface chemistry of ferrihydrite: Part 1. EXAFS studies of the geometry of coprecipitated and adsorbed arsenate. *Geochim. Cosmochim. Acta* **1993**, *57* (10), 2251−2269.
(46) Mikutta, C.; Frommer, J.; Voegelin, A.; Kaegi, R.; Kretzschmar, R. Effect of citrate on the local Fe coordination in ferrihydrite, arsenate binding, and ternary arsenate complex formation. *Geochim. Cosmochim. Acta* **2010**, *74* (19), 5574−5592.
(47) Mikutta, C.; Mandaliev, P. N.; Kretzschmar, R. New clues to the local atomic structure of short-range ordered ferric arsenate from extended X-ray absorption fine structure spectroscopy. *Environ. Sci. Technol.* **2013**, *47* (7), 3122−3131.
(48) Senn, A.-C.; Kaegi, R.; Hug, S. J.; Hering, J. G.; Mangold, S.; Voegelin, A. Composition and structure of Fe(III)-precipitates formed by Fe(II) oxidation in water at near-neutral pH: Interdependent effects of phosphate, silicate and Ca. *Geochim. Cosmochim. Acta* **2015**, *162*, 220−246.
(49) Yang, Y.; Liu, J.; Zhu, R.; Chen, Q.; Wei, H.; Chen, M.; Xian, H.; He, H. Surface-induced oxidation of Mn(II) and crystallization of manganese (hydr)oxides on clay minerals. *Geochim. Cosmochim. Acta* **2023**, *363*, 129−146.
(50) Guinoiseau, D.; Gélabert, A.; Moureau, J.; Louvat, P.; Benedetti, M. F. Zn isotope fractionation during sorption onto kaolinite. *Environ. Sci. Technol.* **2016**, *50* (4), 1844−1852.
(51) Kelly, S. D.; Hesterberg, D.; Ravel, B.; Ulery, A. L.; Richard Drees, L. Analysis of Soils and Minerals Using X-ray Absorption Spectroscopy. In *SSSA Book Series*; Soil Science Society of America, 2008.
(52) Zhou, Q.; Liu, Y.; Li, T.; Zhao, H.; Alessi, D. S.; Liu, W.; Konhauser, K. O. Cadmium adsorption to clay-microbe aggregates: Implications for marine heavy metals cycling. *Geochim. Cosmochim. Acta* **2020**, *290*, 124−136.
(53) Wei, S.; Tan, W.; Zhao, W.; Yu, Y.; Liu, F.; Koopal, L. K. Microstructure, interaction mechanisms, and stability of binary systems containing goethite and kaolinite. *Soil Sci. Soc. Am. J.* **2012**, *76* (2), 389−398.
(54) O'Day, P. A.; Parks, G. A.; Brown, G. E. Molecular structure and binding sites of cobalt(II) surface complexes on kaolinite from X-ray absorption spectroscopy. *Clays Clay Miner.* **1994**, *42* (3), 337−355.
(55) Soltermann, D.; Marques Fernandes, M.; Baeyens, B.; Dähn, R.; Joshi, P. A.; Scheinost, A. C.; Gorski, C. A. Fe(II) uptake on natural montmorillonites. I. Macroscopic and spectroscopic characterization. *Environ. Sci. Technol.* **2014**, *48* (15), 8688−8697.
(56) Liu, X.; Lu, X.; Sprik, M.; Cheng, J.; Meijer, E. J.; Wang, R. Acidity of edge surface sites of montmorillonite and kaolinite. *Geochim. Cosmochim. Acta* **2013**, *117*, 180−190.
(57) Zhang, C.; Liu, X.; Lu, X.; He, M.; Jan Meijer, E.; Wang, R. Surface complexation of heavy metal cations on clay edges: insights from first principles molecular dynamics simulation of Ni(II). *Geochim. Cosmochim. Acta* **2017**, *203*, 54−68.
(58) Jia, Y.; Xu, L.; Wang, X.; Demopoulos, G. P. Infrared spectroscopic and X-ray diffraction characterization of the nature of adsorbed arsenate on ferrihydrite. *Geochim. Cosmochim. Acta* **2007**, *71* (7), 1643−1654.
(59) Ai, Z.; Gao, Z.; Zhang, L.; He, W.; Yin, J. J. Core−shell structure dependent reactivity of $Fe@Fe_2O_3$ nanowires on aerobic degradation of 4-chlorophenol. *Environ. Sci. Technol.* **2013**, *47* (10), 5344−5352.
(60) Peretyazhko, T.; Zachara, J. M.; Heald, S. M.; Kukkadapu, R. K.; Liu, C.; Plymale, A. E.; Resch, C. T. Reduction of Tc(VII) by Fe(II) sorbed on Al (hydr)oxides. *Environ. Sci. Technol.* **2008**, *42* (15), 5499−5506.
(61) Li, F.-b.; Tao, L.; Feng, C.-h.; Li, X.-z.; Sun, K.-w. Electrochemical evidences for promoted interfacial reactions: The role of Fe(II) adsorbed onto γ-Al_2O_3 and TiO_2 in reductive transformation of 2-nitrophenol. *Environ. Sci. Technol.* **2009**, *43* (10), 3656−3661.
(62) Chakraborty, S.; Favre, F.; Banerjee, D.; Scheinost, A. C.; Mullet, M.; Ehrhardt, J.-J.; Brendle, J.; Vidal, L.; Charlet, L. U(VI) sorption and reduction by Fe(II) sorbed on montmorillonite. *Environ. Sci. Technol.* **2010**, *44* (10), 3779−3785.
(63) Chen, P.; Churakov, S. V.; Glaus, M.; Van Loon, L. R. Impact of Fe(II) on 99Tc diffusion behavior in Illite. *Appl. Geochem.* **2023**, *156*, No. 105759.
(64) Schwartz, F. W.; Zhang, H. *Fundamentals of Groundwater*, 2nd ed.; John Wiley & Sons, Inc.: Hoboken, NJ, 2024.
(65) Kaegi, R.; Voegelin, A.; Folini, D.; Hug, S. J. Effect of phosphate, silicate, and Ca on the morphology, structure and elemental composition of Fe(III)-precipitates formed in aerated Fe(II) and As(III) containing water. *Geochim. Cosmochim. Acta* **2010**, *74* (20), 5798−5816.
(66) Ciampi, P.; Esposito, C.; Bartsch, E.; Alesi, E. J.; Rehner, G.; Morettin, P.; Pellegrini, M.; Olivieri, S.; Ranaldo, M.; Liali, G.; Papini,

M. P. A data-driven modeling approach for the sustainable remediation of persistent arsenic (As) groundwater contamination in a fractured rock aquifer through a groundwater recirculation well (IEG-GCW). *Environ. Res.* **2023**, *217*, No. 114827.
(67) He, J.; Charlet, L. A review of arsenic presence in China drinking water. *J. Hydrol.* **2013**, *492*, 79−88.
(68) Catalano, J. G.; Luo, Y.; Otemuyiwa, B. Effect of aqueous Fe(II) on arsenate sorption on goethite and hematite. *Environ. Sci. Technol.* **2011**, *45* (20), 8826−8833.

https://doi.org/10.1021/acs.est.4c01976
Environ. Sci. Technol. 2024, 58, 12123−12134